Contents lists available at ScienceDirect

Transactions of Nonferrous Metals Society of China

36(2026) 470−487

www.tnmsc.cn

Damage evolution mechanism of notch high-cycle fatigue in Ti-55531 alloy with multilevel lamellar microstructure

Zhong ZHANG [a], Chao-wen HUANG [a,*], Chang-sheng TAN [b], Jiang YANG [c], Ming-pan WAN [a], Fei LIU [a,d], Song XIANG [a,**]

[a] National & Local Joint Engineering Laboratory for High-performance Metal Structure Materials and Advanced Manufacturing Technology, Guizhou University, Guiyang 550025, China;

[b] School of Materials Science and Engineering, Xi'an University of Technology, Xi'an 710048, China;

[c] School of Materials and Energy Engineering, Guizhou Institute of Technology, Guiyang 550003, China;

[d] School of Mechanical & Aerospace Engineering, Nanyang Technological University, Singapore 639789, Singapore

Abstract: The interrupted fatigue test method was utilized to investigate the damage evolution mechanism of the notch high-cycle fatigue (NHCF) in Ti-55531 alloy with a multilevel lamellar microstructure. The results reveal that significant microvoids and microcracks predominantly initiate at α/β interfaces under various notch root radii (R). Notably, even under larger R (0.75 mm), mutual interactions of stacking faults (SFs)−deformation twins, twins−twins, and SFs−SFs are observed. Furthermore, with decreasing R (0.34 and 0.14 mm), the volume fraction of SFs escalates significantly and twins are almost absent. Moreover, activated prismatic slip system decreases with a decrease in Schmidt factor and with the further decrease in R. Finally, strain localization near α/β interfaces contributes to the initiation of fatigue microcracks.

Key words: damage mechanism; Ti alloy; interrupted fatigue; crack initiation; stacking fault; twin; prismatic slip system

1 Introduction

Titanium (Ti) and its alloys have been widely applied in aerospace and aviation industry, due to their excellent and well-balanced performance, such as favorable corrosion resistance, preeminent fatigue strength, outstanding specific strength, and extensive service temperature [1−3]. In particular, the Ti alloys with high strength and toughness, and ultimate tensile strength higher than 1100 MPa, have been used as important structural materials in aeronautical industry [1]. Recently, a metastable β-Ti alloy, namely Ti-55531 alloy, with high strength and toughness, high specific strength, and excellent balance between strength and ductility, has been extensively used in manufacturing high-strength critical components such as landing gears and flap tracks in aerospace industry [4−6]. However, the fatigue properties and damage mechanism of Ti-55531 alloys bring forward significant safety concerns during service.

In the past decade, numerous studies have been conducted on the fatigue properties, initiation and propagation of fatigue cracks, as well as rate of fatigue crack propagation in Ti alloys [7,8]. Moreover, several investigations have explored the influence of microstructures on high-cycle fatigue (HCF) and low-cycle fatigue (LCF) deformation, crack initiation and propagation behavior of the

Corresponding author: *Chao-wen HUANG, Tel: +86-18685535799, E-mail: cwhuang@gzu.edu.cn;
**Song XIANG, Tel: +86-18985151196, E-mail: sxiang@gzu.edu.cn

https://doi.org/10.1016/S1003-6326(25)66976-7
Received 8 April 2024; accepted 16 December 2024

Ti-55531 alloy. These studies revealed that both lamellar microstructure (LM) and bimodal microstructure significantly affect the mechanisms of LCF and HCF deformation, as well as fatigue crack initiation in Ti-55531 alloy [6,9−12]. For instance, HUANG et al [11,12] reported that cyclic deformation within LM was primarily governed by slip occurring within elongated secondary α lamellae and $\{10\bar{1}1\}_{\alpha}$ twins. Since the 21st century, numerous studies have been conducted on the fatigue properties of Ti alloys without notch, such as Ti-55531 [9,12,13], TA19 [14] and TC17 [15]. Nonetheless, in the practical engineering applications, most components acquire variable cross-sections or notches with different radii due to special structural requirements. The existence of notches generally leads to stress concentration under loading. However, only a few studies have dealt with the influence of notch size effect on the fatigue properties and fracture mechanisms of the alloys. The notch fatigue issues emerge under cyclic loadings [16], making it desirable to systematically explore the effect of inhomogeneous stress distribution on the fatigue damage process. The stress concentration at the notch root promotes the initiation of fatigue cracks, making the notch become the weak position and starting point of fatigue failure of components [17,18]. For instance, GAO et al [19] investigated the notch fatigue behavior of TC17 alloy in the very high-cycle fatigue (VHCF) regime, and pointed out that the fatigue crack mainly initiated due to the surface stress concentration and defects near the notch root. Furthermore, some scholars argued that the notch and its size significantly influence the fatigue property of aerospace components [20,21]. However, to meet the requirements of structural design, key components in the aerospace field inevitably contain these geometric discontinuity areas or notches. At present, most literature [16,17,19−21] only reports the impact of notch size effect on fatigue properties. Comparatively, studies the micro-mechanism of notch fatigue damage of high strength−toughness Ti alloys with the multilevel LM under different notch root radii (R) have rarely been reported to date. All in all, the notch-induced fatigue problems are common during reliability analysis and structural design for mechanical engineering components [22,23].

Based on the aforementioned exposition, it is crucial to further investigate the notch high-cycle fatigue (NHCF) damage behavior of Ti-55531 alloys with a multilevel LM. During the notch fatigue damage process, different fatigue damage stages are controlled by different microstructural units. Furthermore, after fatigue fracture occurs, the fracture macro-morphology covers some characteristics of the initiation and propagation of fatigue microcracks. Considering these two reasons, in this study, an interrupted fatigue test method was adopted. Combined with NHCF results of Ti-55531 alloy with different R and stress concentration factors (K_t) [24], the numbers of cycles (N) selected for interrupted fatigue test were 3×10^6 and 7×10^6 cycles, respectively. Finally, the evolution process of NHCF damage of Ti-55531 alloy with a multilevel LM was revealed via analysis and characterization methods such as scanning electron microscopy (SEM), transmission electron microscopy (TEM), and electron back-scattered diffraction (EBSD). This study can provide a significant guidance for the design of highly reliable Ti alloy parts with long service life.

2 Experimental

2.1 Materials

A forged bar of Ti-55531 alloy with a diameter of 350 mm (Chinese Western Superconducting Technologies Co., Ltd.) was used as the raw material in this study. The chemical composition of the alloy is presented in Table 1 [24]. To obtain a multilevel LM, all specimens were solution-treated at 860 °C for 2 h, which was followed by furnace cooling to 670 °C for 3 h and then air cooling down to ambient temperature [25]. The microstructure of the multilevel LM of Ti-55531 alloy after heat treatment is illustrated in Fig. 1. After annealing (670 °C), the α lamellae do not completely precipitate. Furthermore, some grain boundaries (GBs) are observed (Fig. 1(a)) and a few dislocations exist inside α lamellae and β matrix, as indicated by TEM image (Fig. 1(b)). Subsequently, the fatigue specimens were machined into notch cylindrical shapes, as shown in Fig. 2(a) [24].

2.2 Interrupted fatigue tests

The NHCF test was conducted on a QBG−100 high-frequency fatigue test machine at ambient temperature. The stress ratio (r), the frequency (f),

Table 1 Chemical composition of as-received Ti-55531 alloy [24] (wt.%)

Al	V	Mo	Cr	Zr	Fe	Si	C	H	O	N	Ti
5.19	4.80	4.90	2.77	1.07	0.07	0.07	0.08	0.001	0.105	0.007	Bal.

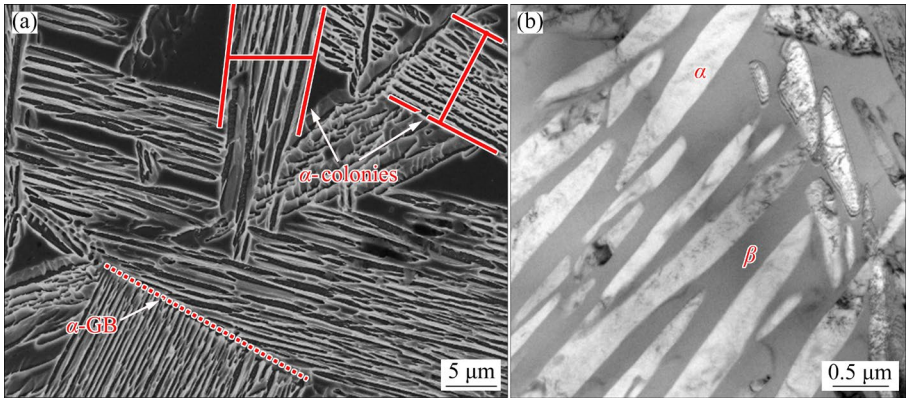

Fig. 1 Microstructure of multilevel LM of Ti-55531 alloy: (a) SEM image; (b) TEM image

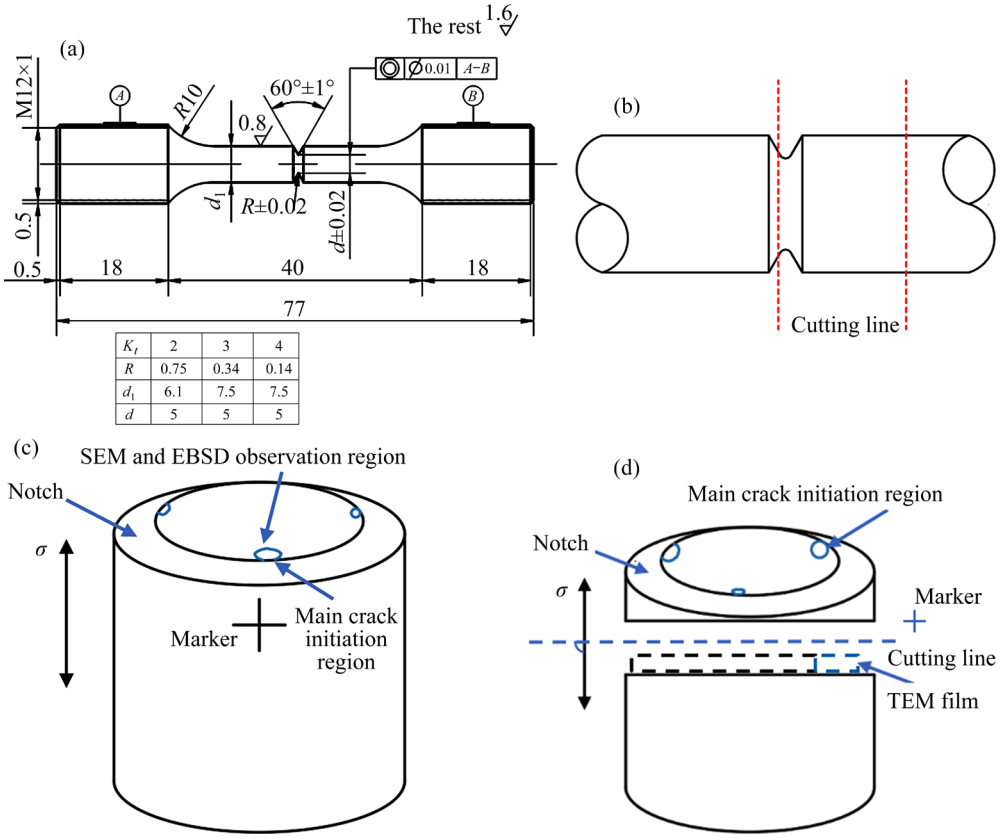

Fig. 2 (a) Dimensions of NHCF sample (all units are in mm, and d_1 and d represent diameters of parallel sections and remaining diameter after notching of sample, respectively) [24]; (b, c, d) Sampling schematic diagrams for characterization analysis after interrupted fatigue test

and the waveform are r=−1, f=120 Hz, and sine wave, respectively. Three groups of fatigue specimens with different notch root radii (R) were subjected to interrupted fatigue experiments. The specific parameters for specimens of each group are as follows: Specimen A: stress concentration factor K_t=2, stress amplitude σ_{-1}=220 MPa, and cycle number N=3×10^6 cycles, Specimen A$_1$: K_t=2, σ_{-1}=220 MPa, and N=7×10^6 cycles; Specimen B: K_t=3, σ_{-1}=130 MPa, and N=3×10^6 cycles, Specimen B$_1$: K_t=3, σ_{-1}=130 MPa, and N=7×10^6 cycles; Specimen C: K_t=4, σ_{-1}=120 MPa, and N=3×10^6 cycles,

Specimen C_1: K_t=4, σ_{-1}=120 MPa, and N=7×10^6 cycles.

2.3 Microstructure characterization and analysis of fatigue fracture

In order to systematically investigate the NHCF damage mechanism and behavior of fatigue microcrack initiation and propagation of Ti-55531 alloy with a multilevel LM under different R, we carefully analyzed the microstructure deformation characteristics of interrupted fatigue specimens in the microcrack initiation region. The specific research methods were as follows: firstly, after completing the interrupted fatigue test, the middle part of specimen was cut with a digital control wire cutting machine (Fig. 2(b)). Secondly, microcrack initiation areas were observed along the notch root by SEM (SUPER40) and the fatigue damage evolution process was analyzed carefully. Finally, the TEM (FEI Tecnai G2 F20) images of the specimens (7×10^6 cycles) were analyzed to study the dislocation change mechanism. TEM films were thinned using an ion-thinning instrument (Gatan 691). For quantitative analysis, multiple micrographs (at least 10 images) of each microstructure were acquired, and microstructural features were determined by using Image Pro Plus 6.0 (IPP 6.0) software. The schematic illustrations of machining procedures of the fractures, and SEM and TEM observation positions of microstructural deformation features are illustrated in Figs. 2(c, d), respectively. Firstly, under the SEM, the location where the crack initiated was identified and marked, as indicated by the "+" in Fig. 2(c). Subsequently, a TEM sample was taken from the marked area for analysis (Fig. 2(d))

To investigate the heterogeneous deformation behavior of the micro-region during the fatigue damage process, the crack initiation region at the notch root was characterized by EBSD test. All EBSD specimens used in this study were polished using argon ion to ensure optimal test results. Prior to EBSD testing, SEM was employed to mark the main crack initiation zone (Fig. 2(c)), and the specimens were polished using an ion grinding instrument (Hitachi Im4000Plus). Subsequently, EBSD test was performed on a Zeiss Gemini SEM 300 instrument equipped with an Oxford C-nano EBSD system using a voltage of 20 keV and a test area size of 800 μm^2 with a step size of 0.19 μm.

3 Results

3.1 Microvoids and microcracks initiation behavior at N=3×10^6 cycles

Figure 3 shows initiation and propagation behavior of microvoids and microcracks at notch root of Specimens A (Figs. 3(a−c)), B (Figs. 3(d−f)) and C (Figs. 3(g−i)), respectively. Figures 3(a−c) illustrate that the initiation of some microvoids and microcracks occurs inside two adjacent α colonies at the notch root of Specimen A during the crack initiation stage of cyclic deformation. The widths of the two α colonies are about 8.07 and 6.12 μm, respectively (Fig. 3(a)). Further analysis shows that numerous microvoids and microcracks initiate at the α/β interfaces (Figs. 3(b, c)). Moreover, a small number of microvoids are also found in the retained β matrix, indicating partial involvement of β phase in cyclic deformation (Fig. 3(b)). Under cyclic loading, these microvoids and microcracks interconnect and propagate from the root of the notch toward the center along the α/β interfaces. However, these formed microcracks are relatively short (mostly less than 0.5 μm in length) and with incomplete connection, showing the characteristics of intermittent distribution (Fig. 3(c)). Some microcracks propagate along the α/β interfaces for a certain distance and then extend through the α lamellae, resulting in the fracture of the α lamellae along the width direction. In another similar α colony, the initiation of numerous microcracks is also observed at the α/β interfaces, and some of the microcracks propagate along the α/β interfaces or cross the α lamellae to form a relatively torsional microcrack propagation path. Moreover, a small number of α lamellae undergo fracture (Fig. 3(c)).

At the initial stage of cyclic deformation for Specimen B, it is evident that microvoids and microcracks are generated within the slightly kinked α colony, measuring ~9.03 μm in width at the notch root (Fig. 3(d)). Some α lamellae adjacent to the α colony also experience varying degrees of distortion deformation, but microvoids and microcracks are absent (Fig. 3(e)). Most of the microvoids and microcracks are observed to nucleate at the α/β interfaces within the slightly twisted and deformed colonies, while a few of them initiate within the α lamellae (Fig. 3(f)).

Evidently, severe torsional deformation occurs

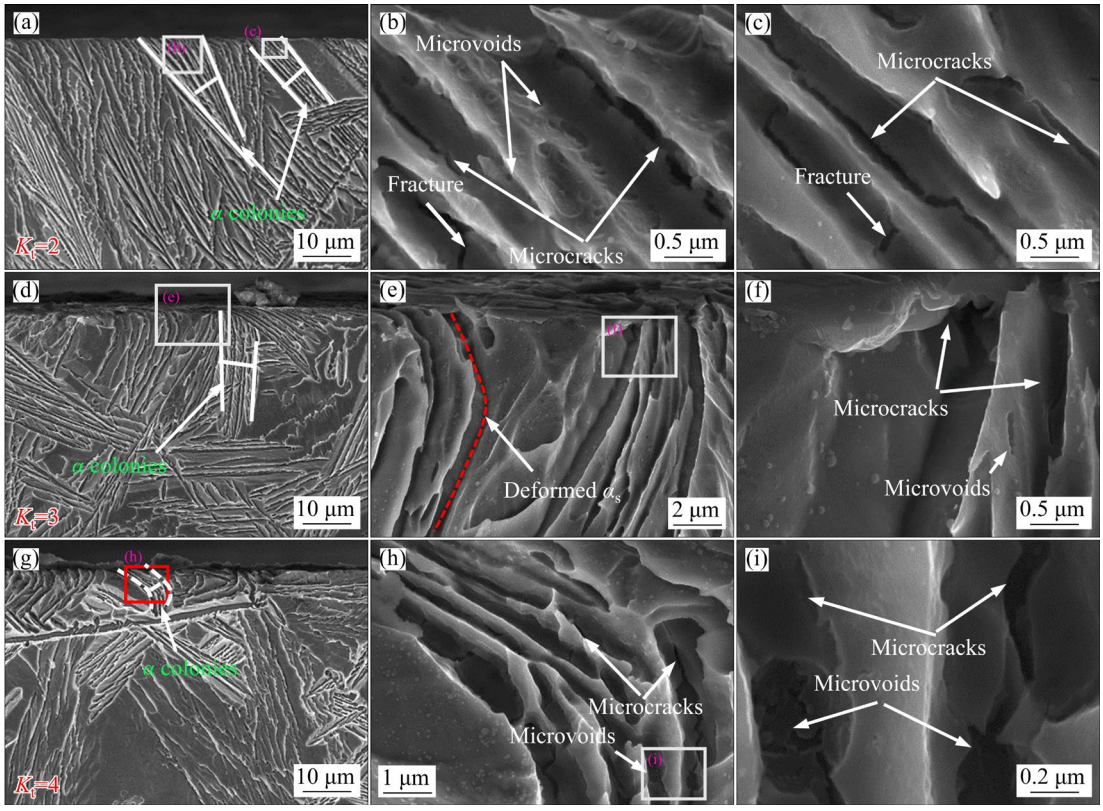

Fig. 3 Microvoid and microcrack characteristics of Specimens A (a−c), B (d−f) and C (g−i): (a, d, g) Deformed α colonies at notch root with different R; (b, e, h) Initiation of microvoids and microcracks within α colonies; (c, f, i) Microvoids and microcracks nucleating into α lamellae and at α/β interfaces

in the α colony at the notch root of Specimen C, with a width of ~3.61 μm, as displayed in Fig. 3(g). In the severely twisted α colony, several microvoids and microcracks initiate at the α/β interfaces, and the diameter of the microvoids is about 130 nm. Moreover, the propagation of microcracks gets interrupted at the GBα (Fig. 3(g)). Most of these microcracks show intermittent distribution at the interfaces. Furthermore, a small amount of α lamellae are also characterized by microcracks, which result in the fracture of α lamellae along the width direction (Fig. 3(h)). Under the action of cyclic loading, these interconnected microvoids and microcracks expand along both twisted and deformed α/β interfaces or traverse across adjacent α lamellae to form a relatively coarse microcrack propagation path (Fig. 3(i)).

3.2 Microcracks initiation and propagation behavior at N=7×10^6 cycles

Figure 4 exhibits the microcrack initiation and propagation characteristics at notch root of Specimens A_1 (Figs. 4(a−c)), B_1 (Figs. 4(d−f)) and C_1 (Figs. 4(g−i)). Figure 4(a) indicates that fatigue microcrack initiation occurs inside the α colony with a width of ~10.62 μm at notch root of Specimen A_1, while numerous microvoids and microcracks initiate at the α/β interfaces. Under prolonged cyclic loading (7×10^6 cycles), fatigue microcracks propagate more completely along the α/β interface or through the α lamellae toward the core of specimen, exhibiting the characteristics of continuous distribution. Moreover, the length of the fatigue microcrack propagation path increases to 27.35 μm (Figs. 4(b, c)). Notably, the fatigue microcracks exhibit the tendency to easily connect and propagate at the α/β interfaces to form longer microcrackc, which leads to higher fatigue crack growth rate and reduces the fatigue life [6,24]. Furthermore, fatigue microcracks also initiate and propagate along the α/β interfaces within the adjacent α colony (Fig. 4(b)). In the fatigue microcrack initiation region, a small quantity of microcracks propagate along the length direction of the α lamellae and fragmentation fracture occurs in partial α lamellae, forming small particles (Fig. 4(c)).

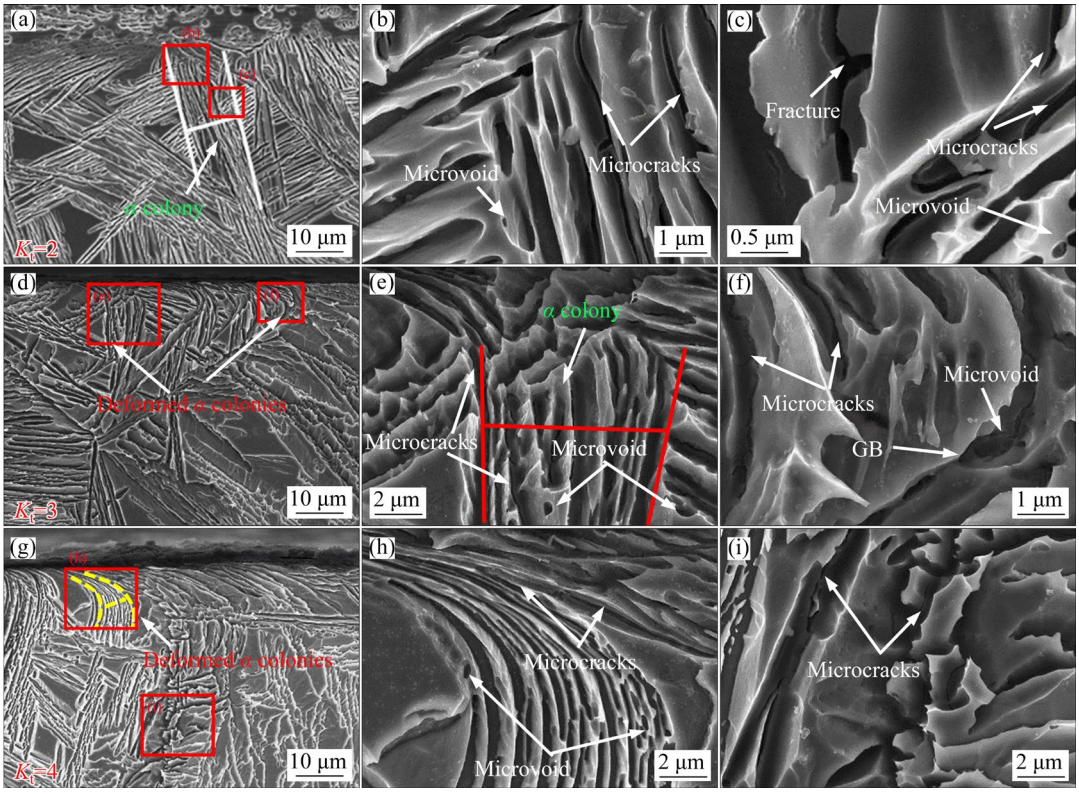

Fig. 4 Microvoid and microcrack characteristics of Specimens A_1 (a−c), B_1 (d−f) and C_1 (g−i): (a, d, g) Deformed α colonies at notch root with different R; (b, e, h) Initiation of microvoids and microcracks within α colonies; (c, f, i) Microvoids and microcracks nucleating into α lamellae and at α/β interfaces, and microcracks propagating along GB and α/β interfaces

Furthermore, some micovoids are formed within certain areas of β matrix as well (Fig. 4(c)), indicating that β matrix also contributes to plastic deformation.

The results reveal that the initiation of fatigue microcracks occurs in two neighboring α colonies at the notch root of Specimen B_1, and the width of α colonies is about 4.78 and 6.65 μm (Fig. 4(d)), respectively. Once microcrack is initiated, it propagates along the α/β interfaces or from the GBs to the center of specimens, and the fatigue microcrack propagation range was found to be ~22.35 μm (Figs. 4(d, e)). The GBs also undergo severe twisting and deformation, and numerous microcracks are initiated at the GBs (Fig. 4(f)).

These figures clearly illustrate that the width of the α colony is about 5.19 μm, which sustains severe torsion deformation at the notch root of Specimen C_1 and it even gets squeezed along the width direction, resulting in significant variations in α colony widths from the specimen surface to subsurface (Figs. 4(g, h)). Under cyclic loading, the microvoids at the interfaces reciprocally connect to form microcracks, and few microcracks are generated inside the α lamellae (Fig. 4(i)). Subsequently, the microcracks propagate along the α/β interfaces to form a longer crack.

3.3 NHCF damage evolution mechanism

In order to further shed light on the influence of R on the fatigue damage evolution of Ti-55531 alloy with multilevel LM, the change of dislocation structure in the microcrack initiation region of the specimens (N=7×10^6 cycles) was thoroughly analyzed by TEM in this section.

Figure 5 shows the dislocation structural characteristics in the microcrack initiation region at the notch root of Specimen A_1 by TEM. The α lamellae mainly bear the cyclic plastic deformation. A high density of dislocations tangle inside α phase and only a few slip lines are present in β phase, as shown in Figs. 5(a, b), indicating that β also bears part of the cyclic plastic deformation. Noteworthy, the α/β interface represents a weak microstructure in multilevel LMs. Dislocations are generated at the α/β interfaces and form numerous parallel dislocation lines (Fig. 5(a)), which subsequently give rise to persistent slip bands (PSBs). Under the continuous action of fatigue loading, the PSBs are

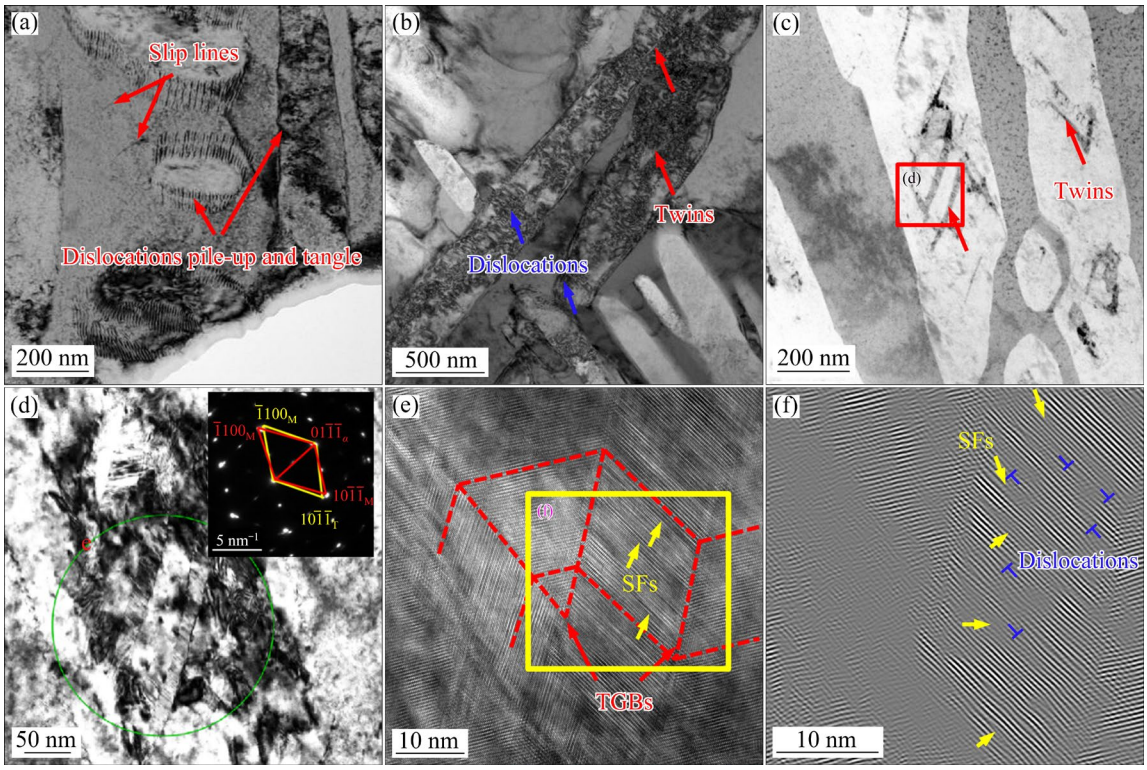

Fig. 5 TEM images of fatigue microcrack initiation region of Specimen A_1: (a) Dislocation lines and dislocation pile-up; (b, c) Twins formed in α lamellae; (d) Selected diffraction pattern of twins; (e) HRTEM images of SFs and twins in (d); (f) IFFT map in yellow rectangle area of (e)

extruded and intruded repeatedly, resulting in grievous stress concentration [26], which accelerates fatigue microvoids, leading to the initiation of microcracks at the α/β interfaces. Furthermore, deformation twins are formed in party of α lamellae (Figs. 5(b−d)) and some SFs are observed in twin plates and around twins (Fig. 5(e)) by high-resolution TEM (HRTEM) image. Finally, the presence of SFs and dislocations in the yellow rectangle area of Fig. 5(e) is confirmed by inverse fast Fourier transform (IFFT) pattern analysis (Fig. 5(f)).

The dislocation structure characteristics of the microcrack initiation region at the notch root of Specimen B_1 are revealed in Fig. 6. The results reveal that a significant number of parallel dislocations are yielded at the α/β interfaces (Figs. 6(a, b)), and the high-density dislocation entanglement occurs in the α lamellae. Moreover, few slip lines are formed in β matrix and a part of the α lamellae undergo breakage (Figs. 6(b, c)). Compared with a larger R (R=0.75 mm), a slight difference is observed in the change of dislocation structure with a smaller R. Owing to the further aggravation of stress concentration at the notch root, a part of the α lamellae undergo shearing to form small nanoparticles, and abundant dislocation entanglements appear at the α/β interfaces and in α lamellae (Fig. 6(b)), which promotes the initiation of fatigue microcracks inside the α lamellae. Detailed analysis reveals the presence of a large number of parallel lines in some α lamellae (Fig. 6(d)), which were confirmed to be basal stacking faults (BSFs) by HRTEM image and selective electron diffraction (Figs. 6(e, f)). The HRTEM and IFFT micrographs reveal that the atoms are clearly disarranged and numerous dislocations exist in the α lamellae. This is the reason that the stress concentration is more serious at the notch root, and SFs are formed in some coarse α lamellae (Fig. 6(d)). During this process, uneven characteristics emerge due to the shear deformation along the α/β interfaces, leading to stress concentration and facilitating the initiation of microvoids and microcracks.

Figure 7 illustrates the dislocation structure characteristics in microcrack initiation region at the notch root of Specimen C_1. The high-density

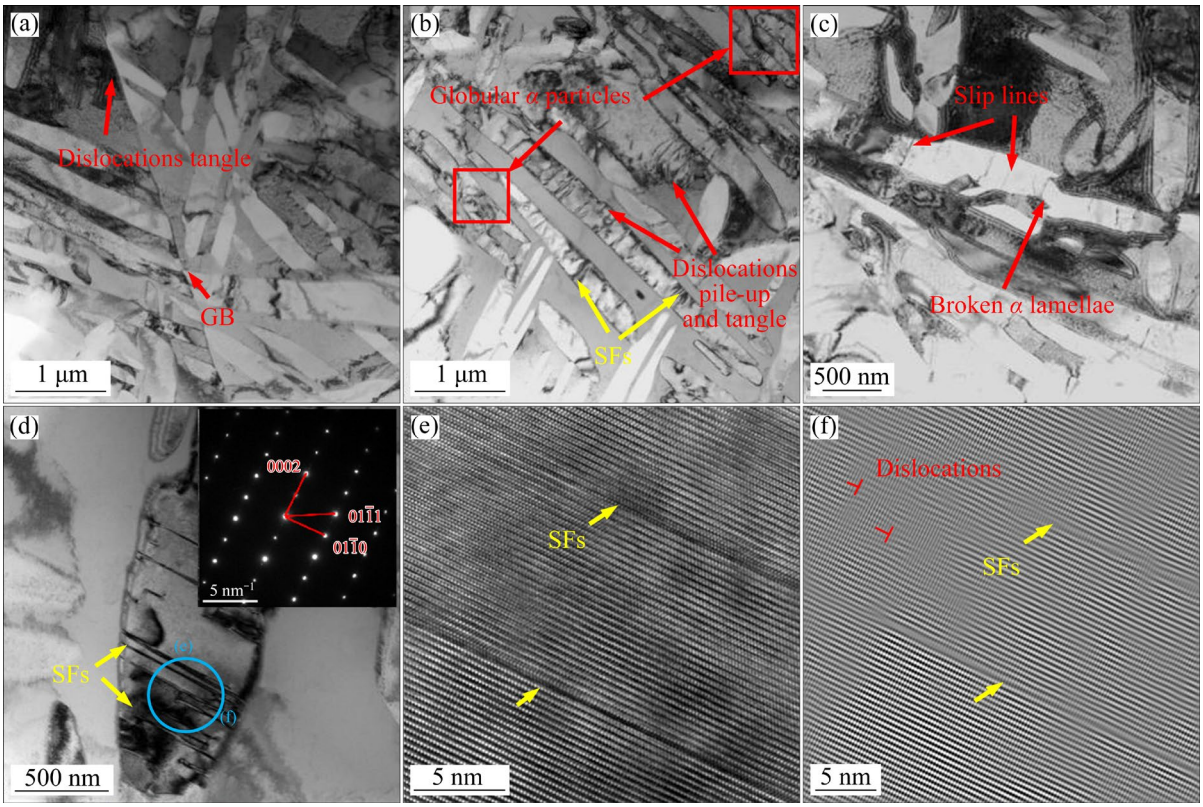

Fig. 6 TEM images of fatigue microcrack initiation region of Specimen B_1: (a) Dislocation tangle; (b) SFs and globular α particles; (c) Dislocation pile-up, dislocation tangle and slip lines; (d) SFs in α lamellae; (e) HRTEM image; (f) IFFT image of (e)

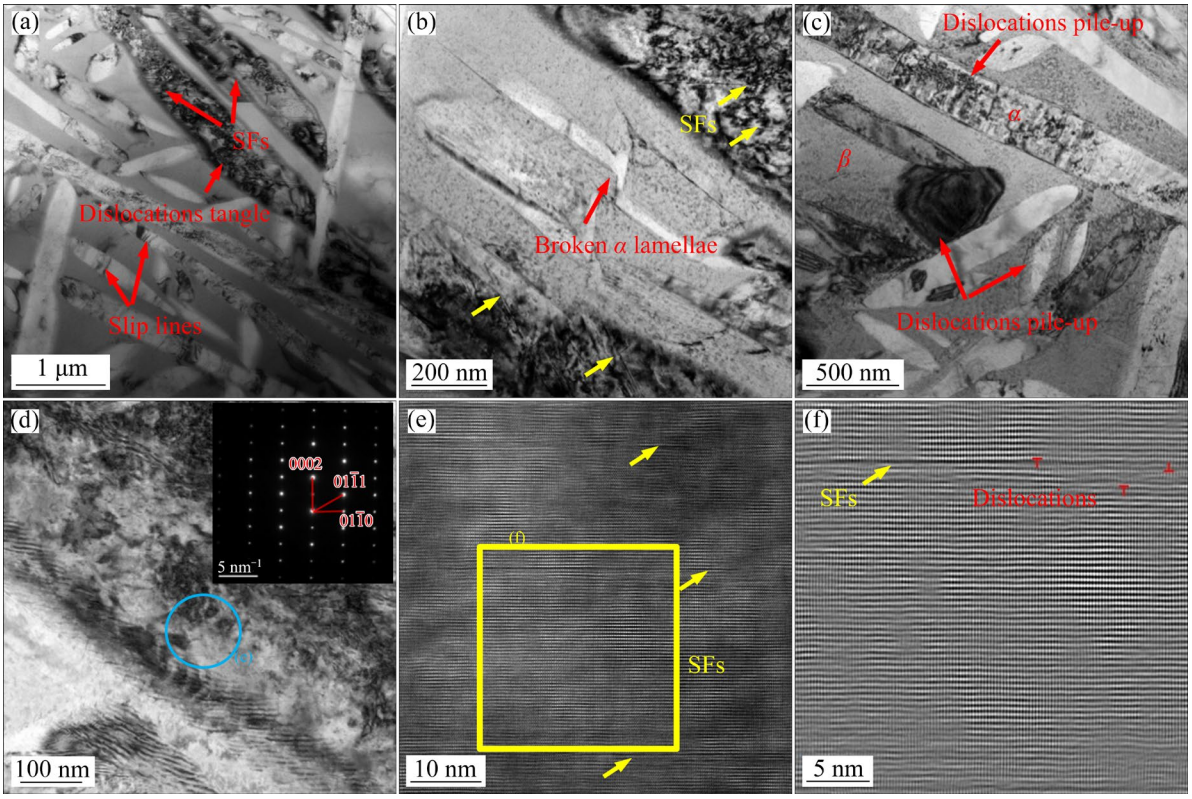

Fig. 7 TEM images of fatigue crack initiation region of Specimen C_1: (a) Dislocation tangle; (b) Breakage of α lamellae; (c) Dislocation pile-up; (d) SFs; (e) HRTEM image; (f) IFFT image in yellow rectangle area of (e)

dislocation tangles are observed in the α lamellae (Figs. 7(a−c)), while a significant number of parallel dislocation lines are present at the α/β interfaces (Fig. 7(d)). Moreover, certain α lamellae exhibit torsion deformation, forming a ladder-like structure that facilitates fatigue microcrack initiation at the α/β interfaces (Fig. 7(b)). This observation is consistent with the analysis of dislocation structure evolution in interrupted fatigue Specimens A_1 and B_1. Furthermore, bits of slip lines and dislocation lines can be observed in some regions of β (Fig. 7(c)). Notably, compared with the specimen with relatively large R (R=0.75 mm), more parallel lines are present in the α lamellae at a smaller R (Fig. 7(d)). These parallel lines were determined to be SFs by selected area diffraction method combined with HRTEM and IFFT images (Figs. 7(e, f)), and numerous dislocations occur within α lamellae (Figs. 7(d, f)). Furthermore, it was also found that the SFs deliver to each other inside α lamellae and stress concentration occurs easily at these interaction points, thereby promoting the microcrack initiation and leading to internal cracking within the α lamellae.

3.4 Heterogeneous deformation behavior in microscopic region of notch root

The EBSD results of the fatigue microcrack initiation region of interrupted Specimen A_1 are presented in Fig. 8. Evidently, α colonies with varying orientations are interleaved, and complete precipitation of α phases within the β matrix is not observed, as indicated by Fig. 8(a). Figure 8(b) displays the pole figures of α and β phases under interrupted fatigue test condition. In the {0001} pole figure of α phase, a maximum intensity texture with a of 100.49 is observed, while a stronger texture with a maximum intensity value of 58.82 is present in the β phase as well. Comprehensive analysis of the Schmidt factor distribution of the prismatic $\{10\bar{1}0\}\langle\bar{1}2\bar{1}0\rangle$ slip system indicates that the Schmidt factor in α phase with high local strain distribution is larger. Moreover, numerous α phases exhibit Schmidt factors greater than 0.42

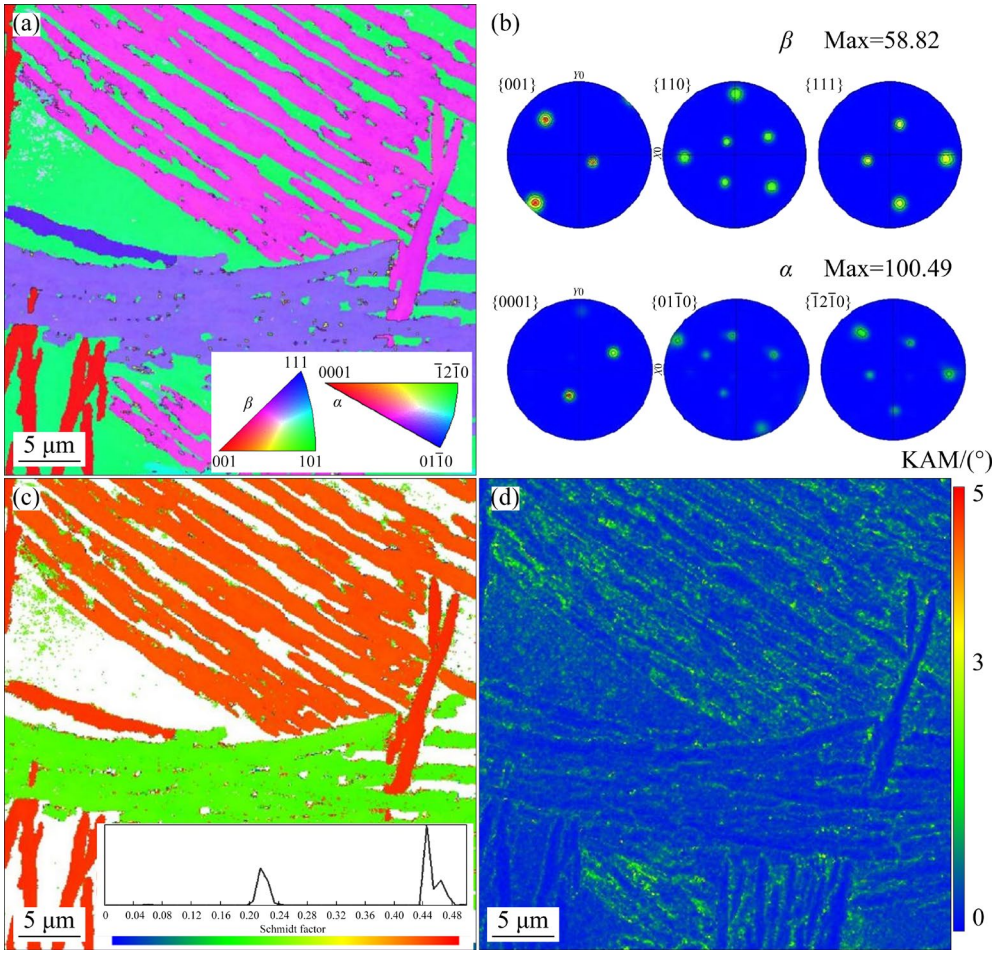

Fig. 8 EBSD results of fatigue microcrack initiation region of Specimen A_1: (a) IPF; (b) PFs; (c) Distribution of Schmidt factor of prismatic slip system; (d) KAM map

(Figs. 8(c, d)). Careful examination of the kernel average misorientation (KAM) map reveals that the strain and high-density dislocations were mainly evenly distributed at the α/β interfaces (Fig. 8(d)). It indicates that the prismatic slip system is mainly involved in plastic deformation during the fatigue process, and large local strain plugging phenomenon can be easily produced at the α phase interface.

Figure 9 illustrates the EBSD results of the fatigue microcrack initiation region of the interrupted fatigue Specimen B_1. α colonies and α lamellae with varying orientations are revealed in the Fig. 9(a). The maximum intensity of α texture decreases significantly to 90.43, which is notably lower than the value observed for Specimen A_1 (100.49). Conversely, the maximum intensity of β texture (59.12) exhibits minimal change (Fig. 9(b)). Comparative analysis of the distribution diagrams for KAM and Schmidt factor indicates that the α phase within regions exhibiting high local strain distribution demonstrates a larger Schmidt factor, thereby facilitating the activation of prismatic slip system (Figs. 9(c, d)). However, the Schmidt factor primarily concentrates in the ranges of 0.06−0.12 and 0.22−0.28, with relatively small values.

Figure 10 shows EBSD results of the fatigue microcrack initiation region of the interrupted fatigue Specimen C_1. The orientations of α lamellae and α colonies are shown in Fig. 10(a). Figure 10(b) evidently indicates that the maximum intensity of α texture significantly increases to 124.26, surpassing the values of Specimens A_1 (100.49) and B_1 (90.43). However, the maximum intensity of β texture remains almost unchanged (Fig. 10(b)) compared to that of Specimens A_1 and B_1 (Figs. 8(b) and 9(b)). With the decrease in R, an increase in stress concentration occurs, leading to a more localized cyclic plastic deformation within a smaller area, thereby intensifying the deformation of α colony. The KAM figure illustrates that strain distribution concentration and dislocation tangles were serious at the α/β interfaces in some microscopic regions, and the α lamellae in these α colonies with severer local strain distribution owned larger Schmidt

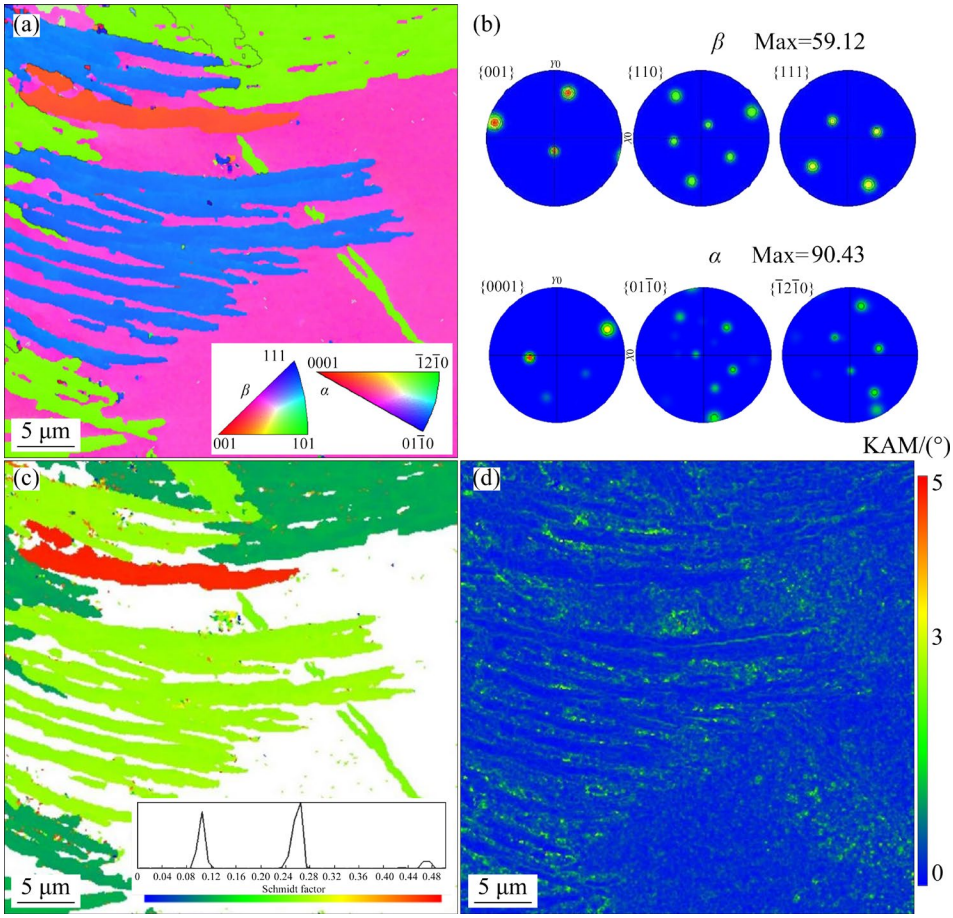

Fig. 9 EBSD results of fatigue microcrack initiation region of Specimen B_1: (a) IPF; (b) PFs; (c) Distribution of Schmidt factor of prismatic slip system; (d) KAM map

factors conducive to the activation of prismatic slip systems $\{10\bar{1}0\}\langle\bar{1}2\bar{1}0\rangle$ (Figs. 10(c, d)).

Furthermore, HAGBs and LAGBs distribution of Specimens A_1−C_1 and the average width of deformed α colony after the interrupted fatigue test were analyzed, as shown in Fig. 11. The number fraction of low-angle GBs (LAGBs, less than 15°) changes with increasing K_t (Fig. 11(a)). The distribution of misorientation reveals that α colony boundaries belong to high-angle GBs (HAGBs, greater than 15°) and α lamellae boundaries belong to LAGBs. Obviously, the number fraction of LAGBs increases while that of the HAGBs decreases. Moreover, Fig. 11(b) illustrates that the average width of deformed α colonies gradually increases with decreasing K_t.

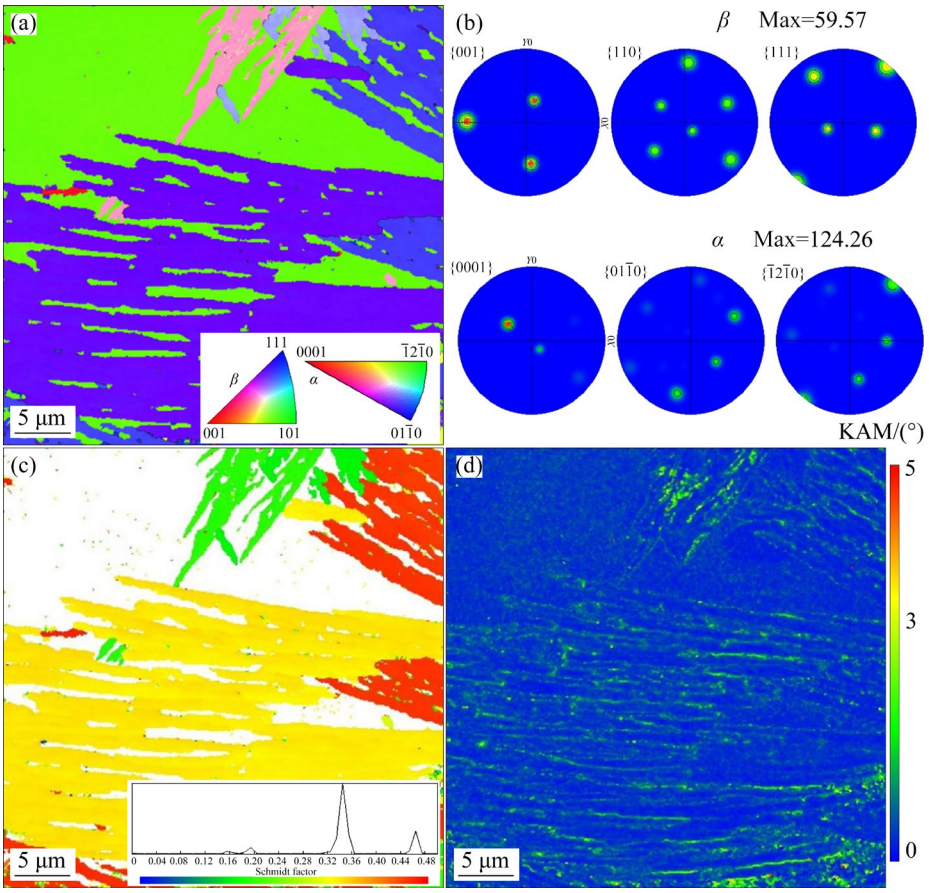

Fig. 10 EBSD results of fatigue microcrack initiation region of Specimen C_1: (a) IPF; (b) PFs; (c) Distribution of Schmidt factor of prismatic slip system; (d) KAM map

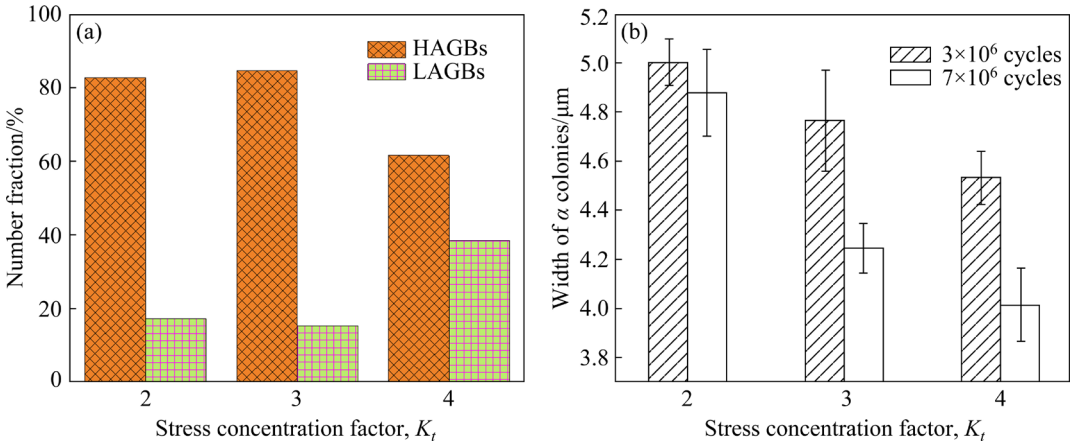

Fig. 11 (a) HAGBs and LAGBs distribution of Specimens A_1−C_1 with K_t values of 2, 3, and 4, respectively; (b) Average width of deformed α colonies after interrupted fatigue test

4 Discussion

4.1 Effect of *R* on fatigue microcrack initiation and propagation

Based on the analysis of initiation and propagation characteristics of microvoids and microcracks of Specimens A−C (Fig. 3), no significant difference exists in the nucleation location of microvoids and microcracks in these specimens with different *R*. The initiation sites for microvoids and microcracks were found at the *α*/*β* interfaces within the *α* colonies as well as inside the *α* lamellae (Fig. 3).

However, noteworthy, the micro-mechanism of fatigue damage varies significantly depending on *R*. Firstly, the size of the cyclic plastic deformation zone exhibits variations with different *R*. Some studies [27,28] have shown that factors affecting the size of the cycle plastic deformation zone at the notch root generally include the applied stress, the yield strength of the material, and the notch shape and dimensions. The present research further reveals distinct differences in *α* colony width within the plastic deformation zone at various *R*. As mentioned earlier, during the initiation stage of microcrack formation, fatigue damage behavior primarily depends on the *R* itself. For instance, smaller *R* results in more pronounced stress concentration and limits plastic deformation to a smaller area. When considering small *R* values (0.34 and 0.14 mm), *α* colony also demonstrates an increased degree of twisting deformation (Figs. 3(b, e, h)).

Notably, the life of fatigue crack initiation stage accounts for most of the entire fatigue life within HCF and VHCF regimes [29,30]. ZHANG et al [24] argued that the initiation of microvoids and microcracks inside the twisted and deformed *α* lamellae or at the *α*/*β* interfaces played a significantly important role in fatigue strength and life. For instance, during the initial stage of fatigue loading, plastic deformation occurs earlier in softer *α* lamellae and *α* colonies due to stress concentration at notch root. With the progress of the deformation process, microvoids and microcracks nucleate within *α* lamellae as well as at the *α*/*β* interfaces within *α* colonies (Figs. 3(c, f, i)). In addition, these microvoids and microcracks interconnect with each other and propagate along the *α*/*β* interfaces or through the *α* lamellae to form relatively long microcracks (Figs. 4(c, f, i)), thus representing a complete process of notch-induced fatigue crack initiation. The mechanism underlying fatigue damage encompasses three stages, i.e. microvoid nucleation, mutual connection between microvoids and microcracks leading to the formation of relatively long cracks, followed by the propagation of these long cracks. This represents a typical mechanism involving the nucleation and aggregation of microvoids and microcracks, resulting in fatigue fracture [31].

The fatigue damage occurs through the early nucleation and propagation of microcracks, which subsequently combine with other factors until they reach a critical length, eventually leading to fatigue fracture [32]. In summary, with the further increase in the cyclic loading, the microcracks at the notch root gradually expand to the center of specimen, forming a larger zone of microcrack growth. Furthermore, more pronounced distortion deformation occurs in *α* colony (Figs. 4 and 11(b)), as indicated by the analysis of microcrack initiation and propagation features of specimens with 7×10^6 cycles. After microcrack initiation, microcracks propagate along the *α*/*β* interfaces or across the *α* lamellae to form long tortuous microcracks.

Moreover, in this group of specimens with *R*= 0.75 mm, *α* colonies with torsion deformation under different fatigue loading cycles (3×10^6 or 7×10^6 cycles) are seldom, which can be attributed to the stress concentration degree at the notch root. By contrast, for the two groups of specimens with *R*= 0.34 and 0.14 mm, fatigue specimens with different cycles were found to possess *α* colonies with a certain degree of torsion deformation. Notably, with decreasing *R*, the average width of deformed *α* colonies gradually decreases (Fig. 11(b)), and numerous microvoids and microcracks initiate within the twisted *α* lamellae and at the *α*/*β* interfaces. According to the literature [24,33], the stress concentration at the *α*/*β* interfaces in Ti alloy makes it a preferred location for the nucleation of microvoids and microcracks.

4.2 Effect of dislocation evolution on microcrack initiation at different *R*

At different *R*, the changing characteristics of dislocations in microcrack initiation region exhibit many similarities. For example, numerous parallel

dislocation lines are generated at the *α*/*β* interfaces. Moreover, high-density dislocation entanglement is yielded inside the *α* lamellae and piles up at *α*/*β* interfaces.

However, as *R* decreases, the stress concentration extent of the notch root increases and the variation in dislocation structure also differs significantly. The specific differences are outlined below: Firstly, under larger *R* (0.75 mm), *α* lamellae do not break or shear to form nanoparticles at microcrack initiation sites. With the increase in the stress concentration of the notch root, some *α* lamellae rupture and even transform into globular particles (*R*=0.34 and 0.14 mm). The analysis of numerous TEM images reveals that greater stress concentration at the notch root leads to the rupture of more *α* lamellae in microcrack initiation zones, and smaller sizes of globular particles are formed by shearing. Secondly, when *R* is larger (0.75 mm), only a few single slip lines are observed in *β* phase. However, with decreasing *R* (0.34 and 0.14 mm), more slip lines are observed in *β* phase (Figs. 6(c), 7(c)), indicating more cyclic plastic deformation undertaken by *β* matrix. Finally, for a larger notch root radius (*R*=0.75 mm), deformation twins of cross and parallel distribution are determined in the *α* lamellae in microcrack initiation region (Figs. 5(b−e)), and numerous SFs are observed in twin plates (Figs. 5(d−f)).

This phenomenon can be attributed to the interaction between twins during cyclic loading or change in strain path, leading to the formation of twin−twin junctions (Figs. 5(b−e)), which further influence continuous twinning, secondary twinning, de-twinning, and cracking [34,35]. During the growth and propagation of deformation twins, twinning-dislocations are often piled up, forming steps [36]. Even under conventional loading, the migration of these steps usually activates the emission of dislocations on basal planes to release stress/strain concentration [37,38]. The emitted dislocations can correspond to partial dislocations if the basal SF energy is reduced, and successive emission of partial dislocations may result in high-density BSFs or phase transformation. Thus, obviously, the propagation and growth of deformation twins inevitably interact with other plastic deformation carriers, such as dislocation slips, SFs, and phase transformation bands if they can be activated simultaneously [39].

HUANG et al [11,12] reported that the cyclic deformation of LM was coordinated by slip within the elongated *α* lamellae and $\{10\bar{1}1\}_{\alpha}$ twins. They found that coarse *α* lamellae in small heterogeneous microstructure region (≤20 μm) and GB_{α} were the preferential HCF crack initiation location for Ti-55531 alloy with LM. BRIFFOD et al [40] found prismatic cracking to be the primary damage mode resulting in fracture compared with basal crack initiation. Nonetheless, these results somewhat conflict with the results of dislocation tangling model reported by BACHE et al [41−43], assuming that cracks always choose the basal slip plane. Furthermore, the uncoordinated deformation between twins and adjacent microstructure also easily leads to the cracking of twin interfaces inside *α* lamellae. The localized shear deformation associated with twinning occurs at low shear stress, leading to mechanical instability [44]. The formation process of twins shears the *α*/*β* interfaces, giving rise to uneven deformation of these interfaces. This causes the stress concentration at the *α*/*β* interfaces and makes preferred location of microcracks initiation [12,45]. However, twins are not generated corresponding to the condition of small *R* (0.34 and 0.14 mm), instead, a portion of SFs is present. Moreover, with further reduction in *R*, stress concentration increases at the notch root, and the density of dislocations and SFs increase significantly. Thus, it was observed that SFs delivered to each other, promoting the fatigue crack initiation (Figs. 5(d)−7(d)). These results are coincident with the results of a previous study [24], shedding light on the generation of SFs causing the twisting deformation of *α*/*β* interfaces, ultimately promoting microcrack initiation at *α*/*β* interfaces.

Moreover, for quantitative analysis of the effect of slips, twins, and SFs on plastic deformation of the NHCF, several TEM images (more than 15 images for a specimen) were obtained and analyzed by using the IPP 6.0 software, and the corresponding results are shown in Fig. 12. These results demonstrate that both *R* and K_t significantly affect the cycle deformation mechanism of the alloy. With the decrease in *R* from 0.75 to 0.14 mm and increase in K_t from 2 to 4, an increase in SFs proportion occurs from 0.4% to 8.9%, while twins gradually decrease (Figs. 5−7). Noteworthy, twinning deformation is influenced by not only material properties, but also temperature

and stress conditions. For instance, Specimen A_1 exhibits greater fatigue strength and loading stress (σ_{-1}=220 MPa), resulting in more twins in the microcrack initiation region compared with other tested specimens. However, it is important to highlight that both twins and SFs can facilitate microcrack initiation at α/β interfaces or within α lamellae, ultimately leading to premature fatigue fracture of these specimens.

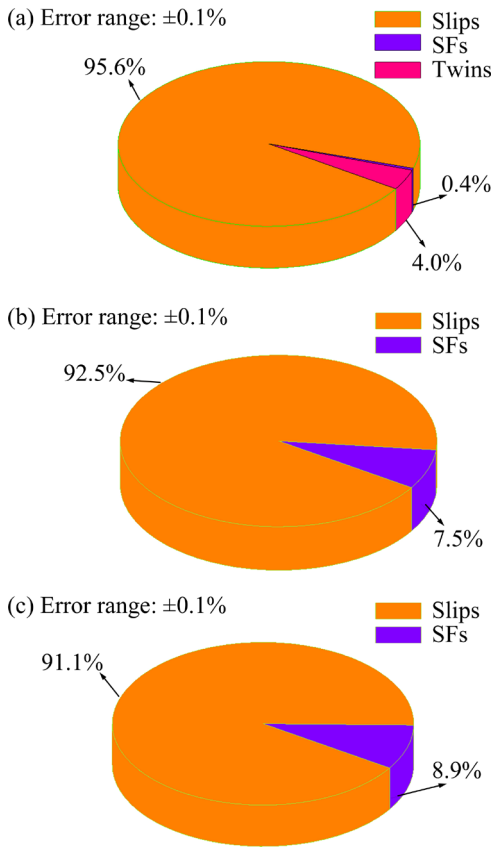

Fig. 12 Proportion of different plastic deformation mechanisms at different K_t and R: (a) R=0.75 mm, K_t=2; (b) R=0.34 mm, K_t=3; (c) R=0.14 mm, K_t=4

4.3 Heterogeneous deformation behavior in microscopic region of notch root

Figures 8(a)−10(a) show the EBSD results, indicating that the α colonies with different orientations are interleaved and some α phases are not precipitated completely in the β matrix. KAM maps were exported for characterizing dislocation density [46], and the KAM values were scalars averaged from 24 nearest neighboring points in EBSD images to represent local misorientation [47].

The KAM maps reveal that strain and high-density dislocations are predominantly distributed at the α/β interfaces (Figs. 8(d)−10(d)), contributing to localized heterogeneous deformation at these interfaces, which facilitate microcrack initiation. The analysis of Schmidt factor distribution of prismatic $\{10\bar{1}0\}\langle\bar{1}2\bar{1}0\rangle$ slip system indicates that the regions with higher local strain distribution exhibit larger Schmidt factors in the α phase (Figs. 8(c, d), 9(c, d), 10(c, d)). However, variations in EBSD test results arise due to different R and K_t values. When R is larger (0.75 mm), strain distribution becomes more uniform, leading to higher Schmidt factors conducive to the activation of prismatic slip system within regions exhibiting higher local strain distribution (0.42) (Figs. 8(c, d)). With the decrease in R, stress concentration and local strain distribution increase accordingly, resulting in reduced Schmidt factors conducive to the activation of prismatic slip system (R=0.34 mm, Schmidt factor ranges of 0.06−0.12 and 0.22−0.28; R=0.14 mm, Schmidt factors between 0.32−0.36), as well as Schmidt factor is relatively small (Figs. 9(c, d), 10(c, d)).

Moreover, in this study, finite element analysis was utilized to reveal that stress concentration increases and the area of plastic deformation zone at the notch root decreases with the decrease in the notch radius, as reported in a previous study [33]. These results reveal that decreasing R leads to the increased stress concentration, limiting plastic deformation within a smaller range while reducing Schmidt factor and activating prismatic slip systems, thereby promoting early initiation of fatigue microcracks within α lamellae. Moreover, LI et al [48] agreed that strain localization in the vicinity of α/β interfaces also promoted local dislocation interaction for strain hardening, resulting in microcrack initiation.

Based on the above-mentioned observations and discussion on microcrack initiation and propagation behavior of Ti-55531 alloy during NHCF damage, the initiation and propagation of microcracks and fatigue damage micro-mechanisms are schematically illustrated in Fig. 13. The results indicate that both the R and K_t significantly influence cyclic plastic deformation as well as initiation of NHCF microcracks in Ti alloys with a multilevel LM. Furthermore, Fig. 13 clearly demonstrates phenomena such as mutual interactions of SFs–deformation twins, twins–twins, and SFs–SFs, promoting microvoid and microcrack initiation at α/β interfaces or within α lamellae.

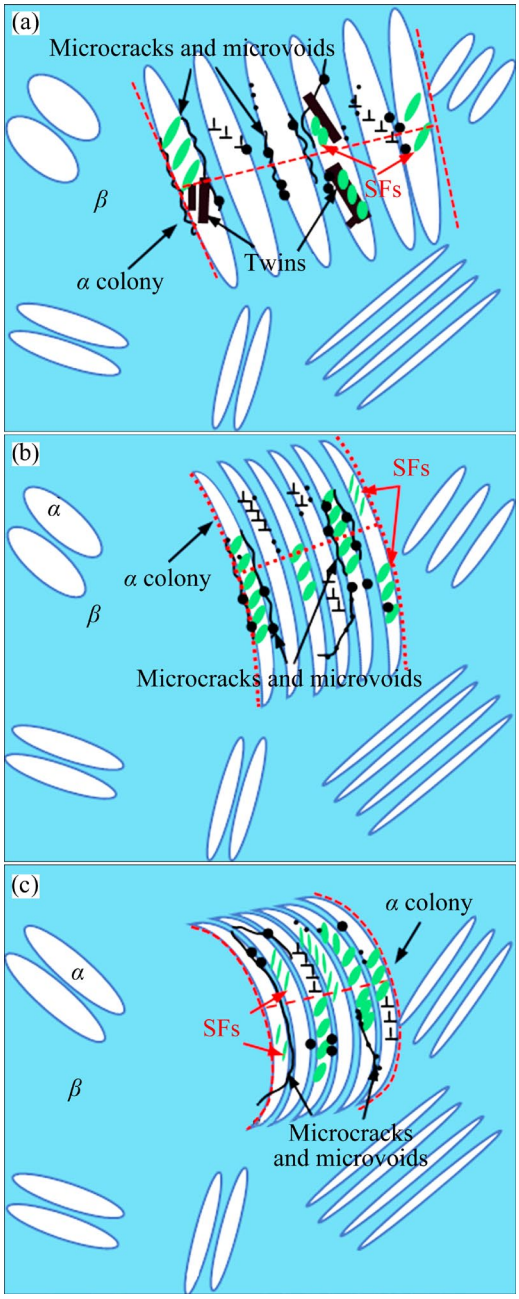

Fig. 13 Mechanism of NHCF microvoids and microcracks initiation under different R and K_t: (a) R=0.75 mm, K_t=2; (b) R=0.34 mm, K_t=3; (c) R=0.14 mm, K_t=4

5 Conclusions

(1) At the early stage of fatigue damage (3×10^6 cycles), microvoids and microcracks initiate at the α/β interfaces and inside the α lamellae in interrupted fatigue specimens with different R. Subsequently, microcracks gradually propagate along the α/β interfaces or through the α lamellae, forming longer microcracks under cyclic loading (7×10^6 cycles). Furthermore, with the decrease in R, K_t increases, the deformation degree of α lamellae and α colonies increases significantly, and the plastic deformation is limited to a smaller area.

(2) The primary cyclic deformation mechanism of Ti-55531 alloy with a multilevel LM is dislocation slipping during the NHCF. Slip bands cut a few α/β interfaces, which show a ladder-like structure due to piling up and tangling of numerous dislocations. Nevertheless, when R is larger (0.75 mm), deformation twins are formed within α lamellae, accompanied by the observation of some SFs in and around twins. Moreover, no twins are observed for small R (0.34 and 0.14 mm). In this case, the proportion of dislocation slipping decreases while that of SFs increases.

(3) At R=0.75 mm, the mutual interactions of SFs−deformation twins, twins−twins, and SFs−SFs promote microvoid and microcrack initiation at α/β interfaces or within α lamellae, but only the SFs−SFs interaction is observed when R=0.34 and 0.14 mm.

(4) With the decrease in R and increase in K_t, the plastic deformation is limited to a smaller range. Consequently, the value of Schmidt factor diminishes and the activated prismatic slip system reduces, which eventually promotes the early initiation and propagation of fatigue microcracks.

CRediT authorship contribution statement

Zhong ZHANG: Methodology, Validation, Formal analysis, Investigation, Data curation, Writing − Original draft, Writing − Review & editing; **Chao-wen HUANG:** Conceptualization, Methodology, Data curation, Supervision, Writing − Original draft, Writing − Review & editing, Funding acquisition; **Chang-sheng TAN:** Validation, Formal analysis, Writing − Original draft; **Jiang YANG:** Conceptualization, Methodology, Writing − Original draft, Writing − Review & editing; **Ming-pan WAN:** Resources, Writing − Original draft; **Fei LIU:** Writing − Original draft; **Song XIANG:** Conceptualization, Methodology, Supervision, Writing − Original draft.

Declaration of competing interest

The authors declare that they have no known competing financial interests or personal relationships that could have appeared to influence the work reported in this paper.

Acknowledgments

This work was supported by the National Natural

Science Foundation of China (Nos. 52061005, 52261025), the Science and Technology Programs of Guizhou Province, China (Nos. YQK[2023]009, CXTD[2023]009), and the Technology Innovation Leading Program of Shaanxi Province, China (No. 2024ZCYYDP92). The authors would like to thank Prof. Yi-long LIANG from Guizhou University. We also thank Dr. Xue-hao ZHENG from ZKKF (Beijing) Science & Technology Company for supporting of TEM analysis.

References

[1] ZHAO Qin-yang, SUN Qiao-yan, XIN She-wei, CHEN Yong-nan, WU Cong, WANG Huan, XU Jian-wei, WAN Ming-pan, ZENG Wei-dong, ZHAO Yong-qing. High-strength titanium alloys for aerospace engineering applications: A review on melting-forging process [J]. Materials Science and Engineering: A, 2022, 845: 143260.

[2] ZHU Wen-guang, MA Chi, ZHANG Cong-hui, HU Kun, ZENG Xiang-kang. Fatigue crack propagation behavior in Ti−6Al−4V alloy with surface gradient structure fabricated by high-energy shot peening [J]. Transactions of Nonferrous Metals Society of China, 2023, 33(10): 3003−3016.

[3] LIU Shi-shuang, CAI Jian-ming, ZHOU Yi, CAO Jing-xia, ZHANG Wang-fei, DAI Sheng-long, HUANG Xu, CAO Chun-xiao. Influence of annealing temperature on microstructural evolution and tensile behavior of Ti−6Al−4V alloy manufactured by multi-directional forging [J]. Transactions of Nonferrous Metals Society of China, 2024, 34(6): 1864−1877.

[4] XIANG Yang, XIANG Wei, YUAN Wu-hua. Flow softening and microstructural evolution of near β titanium alloy Ti-55531 during hot compression deformation in the $\alpha+\beta$ region [J]. Journal of Alloys and Compounds, 2023, 955: 170165.

[5] REN Yu, LI Zheng, ZHANG Zi-yue, CHEN Rong, LI Zi-yong, TAN Cheng-wen, CHEN Peng-wan. Effect of grain size on the shock-induced response and spall fracture behavior of a metastable β titanium alloy subjected to repeated impact [J]. Materials Science and Engineering: A, 2022, 860: 144320.

[6] ZHANG Zhong, HUANG Chao-wen, WEN Xin, WAN Ming-pan, ZHAO Yong-qing, JI Sheng-li, ZENG Wei-dong. Synergistic influence mechanism of microstructure type and loading mode on the long crack propagation in Ti-55531 alloy [J]. Engineering Fracture Mechanics, 2022, 266: 108404.

[7] LONG Jian, ZHANG Lin-jie, ZHU Lei, ZHANG Li-xu, WU Jun, ZHUANG Ming-xiang. Comparison of low-cycle fatigue properties of two kinds of high energy beam welded joints of TC4 alloy [J]. Transactions of Nonferrous Metals Society of China, 2023, 33(11): 3376−3386.

[8] CHEN Kui-wai, PAN Su-ping, LIU Hui-qun, JIANG Yong. Effect of α phase morphology on fatigue crack growth behavior of Ti−5Al−5Mo−5V−1Cr−1Fe alloy [J]. Transactions of Nonferrous Metals Society of China, 2020, 30(9): 2459−2471.

[9] XU Zi-lu, HUANG Chao-wen, WAN Ming-pan, TAN Chang-sheng, ZHAO Yong-qing, JI Sheng-li, ZENG Wei-dong. Influence of microstructure on strain controlled low cycle fatigue crack initiation and propagation of Ti-55531 alloy [J]. International Journal of Fatigue, 2022, 156: 106678.

[10] HUANG Chao-wen, ZHAO Yong-qing, XIN She-wei, ZHOU Wei, LI Qian, ZENG Wei-dong, TAN Chang-sheng. High cycle fatigue behavior of Ti−5Al−5Mo−5V−3Cr−1Zr titanium alloy with bimodal microstructure [J]. Journal of Alloys and Compounds, 2017, 695: 1966−1975.

[11] HUANG Chao-wen, ZHAO Yong-qing, XIN She-wei, TAN Chang-sheng, ZHOU Wei, LI Qian, ZENG Wei-dong. High cycle fatigue behavior of Ti−5Al−5Mo−5V−3Cr−1Zr titanium alloy with lamellar microstructure [J]. Materials Science and Engineering: A, 2017, 682: 107−116.

[12] HUANG Chao-wen, ZHAO Yong-qing, XIN She-wei, TAN Chang-sheng, ZHOU Wei, LI Qian, ZENG Wei-dong. Effect of microstructure on high cycle fatigue behavior of Ti−5Al−5Mo−5V−3Cr−1Zr titanium alloy [J]. International Journal of Fatigue, 2017, 94: 30−40.

[13] XU Zi-lu, HUANG Chao-wen, TAN Chang-sheng, WAN Ming-pan, ZHAO Yong-qin, YE Jun-qing, ZENG Wei-dong. Influence of microstructure on cyclic deformation response and micromechanics of Ti-55531 alloy [J]. Materials Science and Engineering: A, 2021, 803: 140505.

[14] YAO Shu-lei, WANG Gong-yu, YU Hao, WANG Ji, LI Kai-shang, LIU Shuang, ZHANG Xian-cheng, TU Shan-tung. Influence of submerged micro-abrasive waterjet peening on surface integrity and fatigue performance of TA19 titanium alloy [J]. International Journal of Fatigue, 2022, 164: 107076.

[15] LI Gen, SUN Chen-qin. High-temperature failure mechanism and defect sensitivity of TC17 titanium alloy in high cycle fatigue [J]. Journal of Materials Science & Technology, 2022, 122: 128−140.

[16] BRANCO R, PRATES P A, COSTA J D, BORREGO L P, BERTO F, KOTOUSOV A, ANTUNES F V. Rapid assessment of multiaxial fatigue lifetime in notched components using an averaged strain energy density approach [J]. International Journal of Fatigue, 2019, 124: 89−98.

[17] HTOO A T, MIYASHITA Y, OTSUKA Y, MUTOH Y, SAKURAI S. Notch fatigue behavior of Ti−6Al−4V alloy in transition region between low and high cycle fatigue [J]. International Journal of Fatigue, 2017, 95: 194−203.

[18] LEI Yi-wen, MA Guang-lu, LIU Yue, ZHAO Wei, WU Hui-ping, LI Xi-feng. Vibration fatigue properties and deterioration mechanism of diffusion bonded TC4 titanium alloy [J]. Transactions of Nonferrous Metals Society of China, 2024, 34(2): 533−546.

[19] GAO Zhi-yuan, CHEN Xin, ZHU Si-yao, HE Yu-hai, XU Wei. Notch fatigue behavior of a titanium alloy in the VHCF regime based on a vibration fatigue test [J]. International Journal of Fatigue, 2023, 172: 107608.

[20] YU Yi-fei, PEI Xian-jun, WANG Ping, DONG Ping-sha, FANG Hong-yuan. A structural stress approach accounting

for notch effects on fatigue propagation life. Part I: Theory [J]. International Journal of Fatigue, 2022, 159: 106793.

[21] SUSMEL L. Notches, nominal stresses, fatigue strength reduction factors and constant/variable amplitude multiaxial fatigue loading [J]. International Journal of Fatigue, 2022, 162: 106941.

[22] YE Wen-long, ZHU Shun-peng, NIU Xiao-peng, HE Jin-chao, CORREIA J A F O. Fatigue life prediction of notched components under size effect using critical distance theory [J]. Theoretical and Applied Fracture Mechanics, 2022, 121: 103519.

[23] SONG Wei, LIU Xue-song, XU Jie, FAN Yu, SHI Duan-hu, KHOSRAVANI M R, BERTO F. Multiaxial low cycle fatigue of notched 10CrNi3MoV steel and its undermatched welds [J]. International Journal of Fatigue, 2021, 150: 106309.

[24] ZHANG Zhong, HUANG Chao-wen, XU Zi-lu, YANG Jiang, LONG Shao-lei, TAN Chang-sheng, WAN Ming-pan, LIU Dan, JI Sheng-li, ZENG Wen-dong. Influence of notch root radius on high cycle fatigue properties and fatigue crack initiation behavior of Ti-55531 alloy with a multilevel lamellar microstructure [J]. Journal of Materials Research and Technology, 2023, 24: 6293−6311.

[25] HUANG Chao-wen, WANG Feng-mei, WEN Xin, WAN Ming-pan, LEI Min, YE Jun-qin, ZENG Wei-dong. Tensile performance and impact toughness of Ti-55531 alloy with multilevel lamellar microstructure [J]. Journal of Materials Science, 2021, 56(14): 8848−8870.

[26] DODARAN M S, MUHAMMAD M, SHAMSAEI N, SHAO S. Synergistic effect of microstructure and defects on the initiation of fatigue cracks in additively manufactured Inconel 718 [J]. International Journal of Fatigue, 2022, 162: 107002.

[27] TADDESSE A T, ZHU S, LIAO D, HUANG H. Cyclic plastic zone modified critical distance theory for notch fatigue analysis of metals [J]. Engineering Failure Analysis, 2021, 121: 105163.

[28] TADDESSE A T, ZHU S R, LIAO D, KESHTEGAR B. Cyclic plastic zone-based notch analysis and damage evolution model for fatigue life prediction of metals [J]. Materials & Design, 2020, 191: 108639.

[29] SHEN Jie-bin, FAN Hai-dong, WANG Jiang, ZHANG Guo-qian, PAN Rong, HUANG Zhi-yong. Stored energy density research on the fatigue crack initiation at twin boundary and life prediction of Inconel718 superalloy [J]. International Journal of Fatigue, 2023, 171: 107590.

[30] SHEN Jie-bin, FAN Hai-dong, ZHANG Gui-qian, PAN Rong, WANG Jian, HUANG Zhi-yong. Influence of the stress gradient at the notch on the critical distance and life prediction in HCF and VHCF [J]. International Journal of Fatigue, 2022, 162: 107003.

[31] OSOVSKI S, SRIVASTAVA A, WILLIAMS J C, NEEDLEMAN A. Grain boundary crack growth in metastable titanium β alloys [J]. Acta Materialia, 2015, 82: 167−178.

[32] TAN Chang-sheng, SUN Qiao-yan, XIAO Lin, ZHAO Yong-qing, SUN Jun. Cyclic deformation and microcrack initiation during stress controlled high cycle fatigue of a titanium alloy [J]. Materials Science and Engineering: A, 2018, 711: 212−222.

[33] WANG Jiang-xiong, YE Xian-wei, LI Yuan-hui, WAN Ming-pan, HUANG Chao-wen, HUANG Fang, LEI Min, LIU Dan, MA Rui, REN Xian-li. Effect of annealing temperature on mechanical properties of TC21 titanium alloy with multilevel lamellar microstructure [J]. Materials Science and Engineering: A, 2023, 869: 144788.

[34] QIAN Qi, LIU Zheng-qing, JIANG Yong, WANG Yi-ren, AN Xing-long, SONG Min. Basal stacking fault induced twin boundary gliding, twinning disconnection and twin growth in hcp Ti from the first-principles [J]. Transactions of Nonferrous Metals Society of China, 2021, 31(2): 382−390.

[35] YU Qin, WANG Jian, JIANG Yan-yao, MCCABE R J, LI Nan, TOMÉ C N. Twin−twin interactions in magnesium [J]. Acta Materialia, 2014, 77: 28−42.

[36] WU Hai-chen, YU You-xing, BI Xiao-fang. Atomic scale structural characterization of $\{10\bar{1}2\}$ twin boundaries in zinc [J]. Transactions of Nonferrous Metals Society of China, 2018, 28(8): 1538−1542.

[37] PENG Qiu-ming, SUN Yong, WANG Jing, ZU Qun, YANG Meng, FU Hui. Structural characteristics of $\{10\bar{1}1\}$ contraction twin-twin interaction in magnesium [J]. Acta Materialia, 2020, 192: 60−66.

[38] GONG Ming-yu, HIRTH J P, LIU Yue, SHEN Yao, WANG Jiang. Interface structures and twinning mechanisms of twins in hexagonal metals [J]. Materials Research Letters, 2017, 5(7): 449−464.

[39] WEI Bing-qiang, WU Wen-qian, GONG Ming-yu, YU Shu-wei, NI Song, SONG Min, WANG Jian. Influence of lowering basal stacking fault energy on twinning behaviours [J]. Acta Materialia, 2023, 245: 118637.

[40] BRIFFOD F, BLEUSET A, SHIRAIWA T, ENOKI M. Effect of crystallographic orientation and geometrical compatibility on fatigue crack initiation and propagation in rolled Ti−6Al−4V alloy [J]. Acta Materialia, 2019, 177: 56−67.

[41] BACHE M R. A review of dwell sensitive fatigue in titanium alloys: The role of microstructure, texture and operating conditions [J]. International Journal of Fatigue, 2003, 25(9/10/11): 1079−1087.

[42] BACHE M R, COPE M, DAVIES H M, EVANS W J, HARRISON G. Dwell sensitive fatigue in a near alpha titanium alloy at ambient temperature [J]. International Journal of Fatigue, 1997, 19(93): 83−88.

[43] EVANS W J, BACHE M R. Dwell-sensitive fatigue under biaxial loads in the near-alpha titanium alloy IMI685 [J]. International Journal of Fatigue, 1994, 16(7): 443−452.

[44] GRILLI N, COCKS A C F, TARLETON E. Modelling the nucleation and propagation of cracks at twin boundaries [J]. International Journal of Fracture, 2022, 233(1): 17−38.

[45] SANGID M D. The physics of fatigue crack initiation [J]. International Journal of Fatigue, 2013, 57: 58−72.

[46] CHANG Xu-sheng, QI Yu-shi, CHEN Xiao-liang, XIE Zhuan-ye, ZHANG Peng, CHEN Gang. Extra work hardening and activation of softening mechanisms induced by α-β interactions of a metastable-β Ti alloy during subtransus processing [J]. Materials Science and Engineering: A, 2023, 865: 144653.

[47] GEY N, BOCHER P, UTA E, GERMAIN L, HUMBERT M. Texture and microtexture variations in a near-α titanium forged disk of bimodal microstructure [J]. Acta Materialia, 2012, 60(6): 2647−2655.

[48] LI Qiang, HUANG Sheng, ZHAO Ya-kai, GAO Yi-min, RAMAMURTY U. Simultaneous enhancements of strength, ductility, and toughness in a TiB reinforced titanium matrix composite [J]. Acta Materialia, 2023, 254: 118995.

Ti-55531 合金多层次片层组织的缺口高周疲劳损伤演变机制

张 忠[1]，黄朝文[1]，谭长生[2]，杨 江[3]，万明攀[1]，刘 飞[1,4]，向 嵩[1]

1. 贵州大学 高性能金属结构材料与先进制造技术国家地方联合工程实验室，贵阳 550025；
2. 西安理工大学 材料科学与工程学院，西安 710048；
3. 贵州理工学院 材料与能源工程学院，贵阳 550003；
4. School of Mechanical & Aerospace Engineering, Nanyang Technological University, Singapore 639789, Singapore

摘 要：采用中止疲劳实验方法，对具有多层次片层组织的 Ti-55531 合金缺口高周疲劳损伤演化机制进行研究。结果表明，在不同的缺口根半径(R)条件下大量微孔和微裂纹主要萌生在 α/β 界面处。值得注意的是，即使在较大的 R (0.75 mm)条件下观察到层错(SFs)−变形孪晶、孪晶−孪晶和 SFs−SFs 之间的相互作用。此外，随着 R 的减小(0.34 和 0.14 mm)，SFs 的体积分数显著上升，而孪晶几乎消失。随着 R 的进一步减小，激活的柱面滑移系随着施密特因子的减小而减少。最终，α/β 界面附近的应变局部化有助于疲劳微裂纹的萌生。

关键词：损伤机制；钛合金；中止疲劳；裂纹萌生；层错；孪晶；柱面滑移系

(Edited by Wei-ping CHEN)